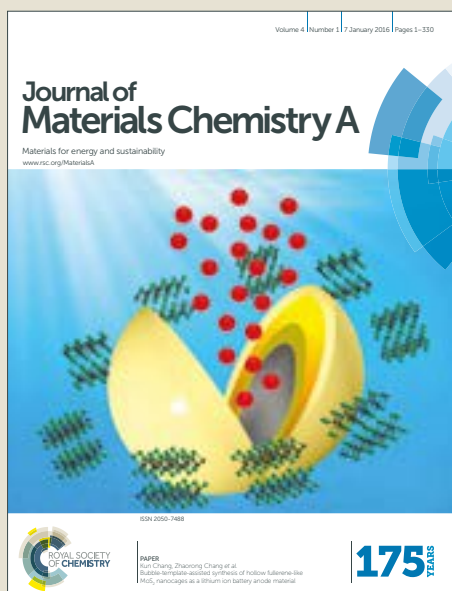


Journal of Materials Chemistry A

Accepted Manuscript



This article can be cited before page numbers have been issued, to do this please use: G. Liu, Z. Sun, X. Zhang, H. Wang, G. Wang, X. Wu, H. Zhang and H. Zhao, *J. Mater. Chem. A*, 2018, DOI: 10.1039/C8TA07162D.



This is an Accepted Manuscript, which has been through the Royal Society of Chemistry peer review process and has been accepted for publication.

Accepted Manuscripts are published online shortly after acceptance, before technical editing, formatting and proof reading. Using this free service, authors can make their results available to the community, in citable form, before we publish the edited article. We will replace this Accepted Manuscript with the edited and formatted Advance Article as soon as it is available.

You can find more information about Accepted Manuscripts in the [author guidelines](#).

Please note that technical editing may introduce minor changes to the text and/or graphics, which may alter content. The journal's standard [Terms & Conditions](#) and the ethical guidelines, outlined in our [author and reviewer resource centre](#), still apply. In no event shall the Royal Society of Chemistry be held responsible for any errors or omissions in this Accepted Manuscript or any consequences arising from the use of any information it contains.



Journal Name

ARTICLE

Vapor-phase hydrothermal transformation of nanosheet array structure Ni(OH)₂ into ultrathin Ni₃S₂ nanosheets on nickel foam for high-efficiency overall water splitting

Received 00th January 20xx,
Accepted 00th January 20xx

DOI: 10.1039/x0xx00000x
www.rsc.org/

Guoqiang Liu^{ab†}, Zhongti Sun^{ct}, Xian Zhang,^{ab} Haojie Wang^{ab}, Guozhong Wang^a, Xiaojun Wu^c, Haimin Zhang^{*a} and Huijun Zhao^{ad}

Electrocatalytic water splitting has been widely accepted as an environmentally friendly approach to generate clean H₂. However, the sluggish oxidation half reaction, namely, oxygen evolution reaction (OER) usually requires high overpotential, which is the bottleneck of high-efficiency overall water splitting to generate H₂. Herein, we report the preparation of ultrathin nanosheet array Ni₃S₂ with 9~14 nm in nanosheet thickness grown directly on commercial Ni foam substrate (Ni₃S₂/NF) by *in-situ* vapor-phase hydrothermal (VPH) transformation of the nanosheet array structure Ni(OH)₂/NF precursor. As a multifunctional electrocatalyst, the as-fabricated Ni₃S₂/NF-2 (VPH time of 2 h) displays excellent electrocatalytic activities toward the hydrazine oxidation reaction (HzOR) with a potential at 0.415 V (vs. RHE) to deliver a current density of 100 mA cm⁻², OER with an overpotential of 425 mV obtaining the same current density, and hydrogen evolution reaction (HER) with an onset potential of -0.05 V (vs. RHE) in 1.0 M KOH media. A two-electrode system is therefore constructed using the Ni₃S₂/NF-2 as both anode and cathode, capable of achieving 100 mA cm⁻² at 0.867 V in 1.0 M KOH with 0.2 M hydrazine. The density functional theory (DFT) calculations reveal that the adsorption of N₂H₄ molecules on the Ni₃S₂ (110) is more thermodynamic favourable than H₂O, thus contributing high HzOR activity.

Introduction

The acquisition of clean hydrogen fuel by the electrocatalytic water splitting has been considered as a promising approach to replace traditional fossil fuels and solve the issues of energy and environment in the future.¹ Two key reaction processes involved in the electrocatalytic water splitting are the hydrogen evolution reaction (HER) and oxygen evolution reaction (OER), which are highly dependent on the electrocatalytic activities of the HER and OER electrocatalysts.² As we know, the HER half-reaction is thermodynamically more favourable than the OER half reaction

during an overall water splitting, because of the kinetically sluggish four electron transfer process of the OER.^{3,4} Therefore, massive efforts have recently been devoted to the development of high-efficiency OER electrocatalysts with low overpotentials.⁵ Although most reported OER electrocatalysts exhibit superior oxygen evolution activities in alkaline media, their catalytic active mechanisms are still unclear, and sometimes controversial owing to the dynamic change of the catalyst atomic structure and composition in alkaline media under the operando conditions. This gives rise to a great difficulty to construct a meaningful atomic structure model of the catalytic active site for the theoretical prediction of the OER active mechanism. In alkaline media, high overpotential of the oxidation half-reaction of an electrocatalyst readily arouses the change of the catalyst atomic structure and composition during electrocatalysis.⁶ Therefore, the development of effective strategies to significantly decrease the overpotential of the oxidation half-reaction using a low-cost and abundant electrocatalyst, is not only favourable for high-efficiency H₂ generation by the electrocatalytic water splitting, but also beneficial for the active mechanism study due to the unchanged catalyst structure and composition at low overpotential under the operando conditions.⁷⁻⁸

^a Key Laboratory of Materials Physics, Centre for Environmental and Energy Nanomaterials, Anhui Key Laboratory of Nanomaterials and Nanostructures, CAS Center for Excellence in Nanoscience, Institute of Solid State Physics, Chinese Academy of Sciences, Hefei 230031, China, *E-mail: zhanghm@issp.ac.cn

^b University of Science and Technology of China, Hefei 230026, China

^c CAS Key Laboratory of Materials for Energy Conversion and Department of Material Science and Engineering, University of Science and Technology of China, Hefei 230026, China

^d Centre for Clean Environment and Energy, Gold Coast Campus, Griffith University, Queensland 4222, Australia

[†] These authors contributed equally in this work.

[†] Electronic Supplementary Information (ESI) available: Supporting SEM image, XPS data, electrochemical measurements of as-prepared samples and calculation results. See DOI: 10.1039/x0xx00000x

Recently, several studies have demonstrated that the electrocatalytic oxidation of fuel molecules (*e.g.*, methanol, ethanol, urea *etc.*) can effectively decrease the overpotentials of the oxidation half-reaction compared to the OER process from water splitting, thus significantly improving the H₂ generation efficiency by utilizing the fuel molecules oxidation reaction to replace the OER process for the overall water splitting.⁹⁻¹² This concept is also extended to electrocatalytically synthesize high value-added chemicals.⁷⁻¹¹ Owing to strong reductive capability (-0.33 V vs. RHE) and high energy density (5.5 kWh L⁻¹), hydrazine (N₂H₄) has been widely recognized as a promising liquid fuel for direct hydrazine fuel cells (DHFCs) with a theoretical voltage of ~1.56 V and environmentally friendly oxidation products (nitrogen and water).^{13,14} The introduction of hydrazine oxidation reaction (HzOR) in DHFCs can significantly decrease the overpotential of the oxidation half-reaction, possibly meaning that the integration of the HzOR process into an overall water splitting may be very favourable for the electrocatalytic H₂ generation. However, the realization of these purposes is highly dependent the HzOR activity of an electrocatalyst, of course, the corresponding HzOR active mechanism is also worthy of in-depth investigation and disclosure.

Up to now, transitional metal (*e.g.*, Co, Ni) based materials have been studied intensively as the HER and OER electrocatalysts for water splitting to generate H₂ due to their high efficiency, low cost and resource abundance.^{15,16} Herein, nanosheet-structured Ni(OH)₂ directly grown on commercial nickel (Ni) foam (NF) was first fabricated by a facile hydrothermal method. Subsequently, the as-fabricated Ni(OH)₂/NF was further used as precursor to *in situ* transform into ultrathin nanosheet-structured Ni₃S₂/NF using thiourea as vapor reactant resource (*e.g.*, H₂S) through a vapor-phase hydrothermal (VPH) method developed previously by our group (Fig. S1, ESI[†]).^{12,17-19} The results demonstrate that the resultant Ni₃S₂/NF-2 sample obtained at 220 °C under VPH conditions with a reaction time of 2 h exhibits ultrathin nanosheet array structure with thickness of 9~14 nm in nanosheet, vertically grown on the NF substrate, significantly different from its precursor Ni(OH)₂/NF with the nanosheet thickness of 130~180 nm. Such ultrathin Ni₃S₂ nanosheet array structures on the NF substrate are very favourable for the exposure of catalytic active sites for high-efficiency electrocatalysis.^{20,21} As a result, the Ni₃S₂/NF-2 displays superior trifunctional electrocatalytic activities of HER, OER and HzOR with the onset potentials of -0.05, 1.52 and 0.10 V (vs. RHE) in 1.0 M KOH solution, respectively. Apparently, the introduction of 0.2 M hydrazine in 1.0 M KOH results in significantly decreased oxidation potential using the Ni₃S₂/NF-2 electrode compared to the OER process from the electrocatalytic water oxidation. Moreover, only 0.415 V (vs. RHE) of the oxidation potential in 0.2 M hydrazine+1.0 M KOH using the Ni₃S₂/NF-2 electrode can afford a high current density of 100 mA cm⁻². Owing to superior HER and HzOR activities, the Ni₃S₂/NF-2 was concurrently used as the cathode and anode material to construct a two-electrode system for the overall water splitting, delivering a high current density of 100 mA cm⁻² at only 0.867 V in 1.0 M KOH with 0.2 M hydrazine. Comparatively, the applied voltage is 2.01 V for such two-electrode

system to achieve the current density of 100 mA cm⁻² in 1.0 M KOH without the introduction of hydrazine. The superior HzOR activity on the Ni₃S₂/NF-2 has been discussed on the basis of the experimental and theoretical calculations results. The density functional theory (DFT) calculations indicate that N₂H₄ molecule owns much stronger interaction with the Ni₃S₂ (110) (adsorption energy of -1.41 eV) than that (adsorption energy of -0.82 eV) of H₂O on the Ni₃S₂ (110), thus contributing superior HzOR activity.

Experimental section

Chemicals

Nickel (Ni) foam, hydrochloric acid (HCl) and potassium hydroxide (KOH) were provided by Sinopharm Chemical Reagent Co., Ltd. Thiourea (CH₄N₂S) was purchased from Aladdin Industrial Corporation. Commercial carbon fiber cloth was supplied by Shanghai Hesun Electric Co., Ltd, China. All chemicals were used as received without any further treatment. All experiments were performed at room temperature (~25 °C).

Fabrication of nanosheet-structured Ni(OH)₂/NF

Nanosheet-structured Ni(OH)₂/NF was fabricated according to a previously reported method.²² Prior to the fabrication, the commercial Ni foam (4.0×2.0×0.16 cm³) was sequentially washed in 3.0 M HCl solution, ethanol and deionized water under ultrasound conditions. Subsequently, the pre-cleaned Ni foam was immersed into a 50 mL of HCl solution with pH=3.0, and then the above mixture was transferred into 80 mL of Teflon-lined stainless-steel autoclave. The autoclave was maintained at 180 °C for 6 h. After cooling down to room temperature, the hydrothermal treated Ni foam was adequately washed for several times with deionized water and dried at 60 °C in vacuum for overnight. The finally obtained sample was denoted as Ni(OH)₂/NF.

Fabrication of ultrathin nanosheet-structured Ni₃S₂/NF

Ultrathin nanosheet-structured Ni₃S₂/NF samples were fabricated through a vapor-phase hydrothermal (VPH) method reported previously by our group.^{12,17-19} In a typical fabrication, the VPH reaction was performed in a Teflon-lined stainless-steel autoclave (80 mL) with Ni(OH)₂/NF precursor placed above liquid level of 10 mL of 1.5 M thiourea solution (Fig. S1, ESI[†]). The VPH reaction was carried out at 220 °C for 1, 2 and 3 h. Finally, the obtained products were washed with deionized water for several times and then dried at 80 °C in vacuum for overnight. The as-fabricated samples were denoted as Ni₃S₂/NF-1, Ni₃S₂/NF-2 and Ni₃S₂/NF-3 with different reaction times. The Ni₃S₂ loading amount on Ni foam substrate is estimated to be ~2.5 mg cm⁻², ~1.4 mg cm⁻² and ~1.3 mg cm⁻² for Ni₃S₂/NF-1, Ni₃S₂/NF-2 and Ni₃S₂/NF-3, respectively.

Characterization

X-ray diffraction (XRD) patterns of the samples were identified on a Philips X-Pert Pro X-ray diffractometer with Cu K α radiation ($\lambda_{K\alpha 1}$ = 1.5418 Å). The morphological and structural information of the samples was obtained by field emission scanning electron microscopy (FE-SEM, SU 8020) with an accelerated voltage of 10 kV and transmission electron microscopy (TEM, JEOL 2010) with an

accelerated voltage of 200 kV. X-ray photoelectron spectroscopy (XPS) analysis of the samples was performed on an ESCALAB 250 X-ray photoelectron spectrometer (Thermo, USA) equipped with Al $K\alpha_{1,2}$ monochromatized radiation at a 1486.6 eV X-ray source. Raman spectra of the samples were obtained via a LabRAM HR800 confocal Raman microscope (Horiba Jobin Yvon) with an Ar ion laser operating at 632 nm.

Electrochemical measurements

The electrochemical measurements of the as-fabricated samples for the hydrogen evolution reaction (HER), oxygen evolution reaction (OER) and hydrazine oxidation reaction (HzOR), were investigated on a CHI760D (CH Instruments, Inc., Shanghai, China) electrochemical workstation, using a traditional three-electrode system composed of the as-fabricated catalyst as the working electrode, and a Hg/HgO electrode and a commercial carbon cloth as the reference electrode and counter electrode. The as-prepared samples were cut into 1 cm \times 2 cm as the working electrodes. For comparison, the commercial RuO₂ and Pt/C were coated on commercial Ni foam for measurements. The linear sweep voltammetry (LSV) curves were recorded in 1.0 M KOH solution with (HzOR) or without (OER and HER) 0.2 M hydrazine at a scan rate of 5.0 mV s⁻¹. The electrochemical impedance spectroscopy (EIS) analysis of the samples was performed in a frequency range from 100,000 Hz to 0.1 Hz at 1.55 V (vs. RHE) with 5.0 mV amplitude using a CHI 760D electrochemical workstation.

Calculation details

All the calculations were performed by spin-polarized

density functional theory, implemented by Vienna Ab-initio Simulation Package (VASP)^{23,24} with projector augmented wave (PAW) method.²⁵ The electronic exchange-correlation interactions were treated with Perdew-Burke-Ernzerhof (PBE) functional.²⁶ The plane wave energy cutoff was set to be 400 eV, the job was stopped until the total energy and force with less than 10⁻⁵ eV and -0.01 eV/Å. The Brillouin zone integrations with Monkhorst-Packing method were used 4 \times 4 \times 1 and 8 \times 8 \times 1 k-points for optimization and static computations.²⁷ We built (1 \times 1) Ni₃S₂ (110) surface with three layers, one layer was composed of three Ni₃S₂ unit. The third layer was fixed, other layers and adsorbates was allowed to relax fully. There are low and high coordinate Ni atoms in the surface named as Ni-1 and Ni-2 in Fig. S2 (ESI[†]), respectively. The vacuum space is 15 Å. Charge transfer between molecules and Ni₃S₂(110) surface was analyzed through bader charge analysis.²⁸

According to the types of Ni atoms, we considered two adsorption configurations of N₂H₄ and H₂O molecules on the Ni₃S₂(110) surface in Fig. S3 (ESI[†]), respectively. The adsorption energies of N₂H₄ and H₂O molecules were calculated by below formula:

$$E_{\text{ads}} = E_{\text{total}} - E_{\text{surf}} - E_{\text{mole}}$$

where E_{total} and E_{surf} are the total energy of Ni₃S₂(110) surface with and without molecule, E_{mole} is the energy of N₂H₄ and H₂O. Positive and negative values indicate endothermic and exothermic, respectively.

For H₂O, the adsorption energy of H₂O-1 with -0.82 eV on the Ni-1 site is lower than H₂O-2 with -0.17 eV on the Ni-2 site by 0.65 eV. The Adsorption energy of N₂H₄-2 with single-dendate on Ni-1 site is a little lower than N₂H₄-1 with bidendate on Ni-1 and Ni-2 sites by 0.06 eV.

Results and discussion

In this work, Ni(OH)₂ nanosheet arrays were first grown on the pre-cleaned commercial nickel foam (NF) substrate by a simple hydrothermal method.²² Subsequently, the nanosheet array structure Ni(OH)₂/NF as precursor was *in situ* transformed into

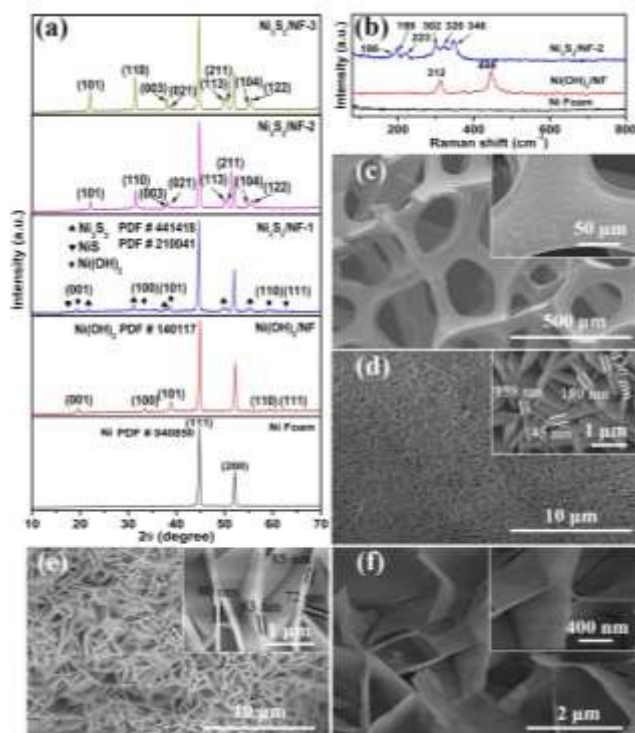


Fig. 1 (a) XRD patterns of the as-prepared samples. (b) Raman spectra of NF, Ni(OH)₂/NF and Ni₃S₂/NF-2. SEM images of (c) NF, (d) Ni(OH)₂/NF, (e) Ni₃S₂/NF-1 and (f) Ni₃S₂/NF-2.

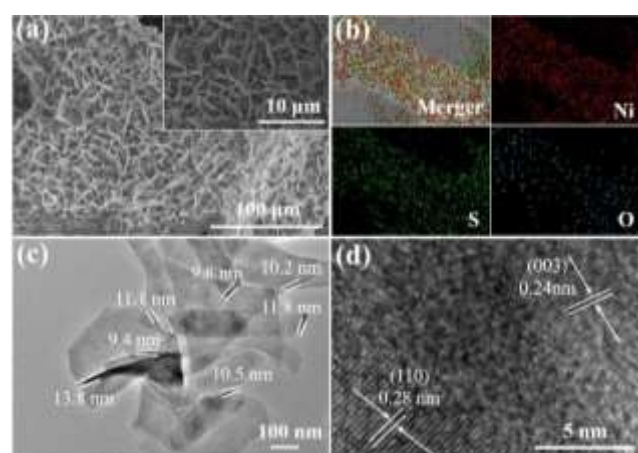


Fig. 2 (a) SEM images and (b) EDS elemental mapping images of Ni₃S₂/NF-2. (c) TEM image and (d) HR-TEM image of Ni₃S₂/NF-2.

ultrathin nanosheet array structure Ni₃S₂/NF by a vapor-phase hydrothermal (VPH) method.^{12,17-19} At 220 °C, thiourea can decompose to produce gaseous products such as H₂S, which further react with Ni(OH)₂ nanosheet array structures on the NF substrate to *in situ* reconstruct and form the ultrathin Ni₃S₂ nanosheet arrays on the NF. The formed ultrathin Ni₃S₂ nanosheet arrays are very favourable for the exposure of the catalytic active sites and electron transfer for high-efficiency electrocatalysis. Fig. 1a shows the XRD patterns of NF substrate, Ni(OH)₂/NF, Ni₃S₂/NF-1, Ni₃S₂/NF-2 and Ni₃S₂/NF-3. As shown, the NF substrate exhibits two strong diffraction peaks at 2θ=44.3° and 51.6°, which can be due to the (111) and (200) planes of the metallic Ni (JCPDS no. 04-0850).²⁹ Besides of two characteristic diffraction peaks of metallic Ni, other five peaks at 2θ=19.3°, 33.1°, 38.6°, 59.1° and 62.7° can be clearly observed for the Ni(OH)₂/NF, corresponding to the (001), (100), (101), (110) and (111) planes of Ni(OH)₂ (JCPDS no. 14-0117).³⁰ Interestingly, it can be seen that the Ni₃S₂/NF-1 sample exhibits the diffraction peaks of metallic Ni, Ni(OH)₂ and Ni₃S₂, indicating an incomplete transformation of Ni(OH)₂ to Ni₃S₂ with a short VPH reaction time of 1 h. However, besides of the diffraction peaks of metallic Ni, the Ni₃S₂/NF-2 and Ni₃S₂/NF-3 samples display the diffraction peaks at 21.7°, 31.1°, 37.7°, 38.2°, 49.7°, 50.1°, 54.6° and 55.4°, indexed to (101), (110), (003), (021), (113), (211), (104) and (122) planes of the hexagonal phase Ni₃S₂ (JCPDS no. 44-1418).^{31,32} No diffraction peaks of Ni(OH)₂ can be detected for the Ni₃S₂/NF-2 and Ni₃S₂/NF-3 samples, suggesting a complete transformation of Ni(OH)₂ to Ni₃S₂ with a long VPH reaction time (2 h or 3 h). Fig. 1b shows the Raman spectroscopy analysis of NF substrate, Ni(OH)₂/NF and Ni₃S₂/NF-2 samples. As we know, metallic Ni as typical metallic crystal, no Raman peaks can be observed. However, the Ni(OH)₂/NF shows two characteristic Raman peaks at 312 and 446 cm⁻¹, which are attributed to an E-type vibration of the Ni(OH)₂ lattice and Ni-O stretching, respectively.³³ After the VPH treatment, the Ni₃S₂/NF-2 exhibits six peaks at 186, 199, 223, 302, 320, and 346 cm⁻¹, which can be ascribed to the different vibration types of Ni₃S₂.^{34,35} The above results further confirm the formation of Ni₃S₂ on the NF substrate by the VPH transformation of Ni(OH)₂ with a long reaction time (e.g., 2 h). Fig. 1c shows the SEM image of commercial NF substrate, exhibiting a relatively smooth surface structure. After a hydrothermal treatment of NF substrate in HCl solution with a pH of 3.0 at 180 °C for 6 h, large-scale Ni(OH)₂ nanosheet array with nanosheet thickness of 130~180 nm can be observed on the NF substrate for the Ni(OH)₂/NF (Fig. 1d). The nanosheet thickness is decreased to 70~90 nm for the Ni₃S₂/NF-1 sample (Fig. 1e). Further increasing the VPH reaction time to 2 h, the Ni₃S₂/NF-2 presents the nanosheet thickness decreased to 9~14 nm (Fig. 1f), which can be further confirmed by the following TEM characterization. After the VPH reaction of 3 h (Fig. S4, ESI[†]), the Ni₃S₂/NF-3 displays ultrathin and size-decreased nanosheet structures on the NF with damaged morphologies, possibly decreased the active species for the electrocatalysis. The above results demonstrate that the decrease of the nanosheet thickness and size with the reaction time may mean partial Ni reaction resource running off into the aqueous phase during the VPH transformation of Ni(OH)₂ to Ni₃S₂.

The low-magnification SEM images (Fig. 2a) of Ni₃S₂/NF-2 indicate that the ultrathin nanosheet arrays can be maintained well on the NF, which is critically important for its electrocatalysis application when directly used as the electrode. Fig. 2b shows the energy dispersive spectroscopy (EDS) element mapping analysis of the Ni₃S₂/NF-2. Clearly, the element mapping results indicate that the Ni, S and O elements are homogeneously distributed over the entire Ni₃S₂/NF-2, verifying the formation of nickel sulfide. Moreover, the O element may be from the substrate of NF under 220 °C for 2 h reaction. Fig. 2c and Fig. S5 (ESI[†]) shows the different-magnification TEM images of Ni₃S₂/NF-2. The ultrathin nanosheet structures can be clearly observed with Ni₃S₂ nanosheet thickness of 9~14 nm.^{36,37} The high-resolution TEM image (Fig. 2d) of an individual nanosheet shows the lattice fringe spacings are 0.24 and 0.28 nm, corresponding to the (003) and (110) crystallographic planes of the hexagonal Ni₃S₂.^{38,39} As shown in Fig. S6 (ESI[†]), the thickness of Ni₃S₂ nanosheet array is 4.8 μm, 4.2 μm and 3.7 μm for Ni₃S₂/NF-1, Ni₃S₂/NF-2 and Ni₃S₂/NF-3, respectively. The formation of ultrathin Ni₃S₂ nanosheet arrays not only validates the superiority of the *in-situ* VPH transformation method in regulating the crystal phase and composition of nanostructure material, but also possibly provides well-exposed Ni- and S-related catalytic active sites and high conductivity for high-efficiency electrocatalysis.

Recently, Ni-based hydroxides and sulfides have been widely investigated for the electrocatalysis, exhibiting superior electrocatalytic activities of the oxygen evolution reaction (OER).^{17,21,29,38,40-43} In this work, the as-fabricated Ni(OH)₂/NF, Ni₃S₂/NF-1, Ni₃S₂/NF-2 and Ni₃S₂/NF-3 samples were used as the electrocatalysts for evaluating their OER activities in 1.0 M KOH electrolyte. Fig. 3a shows the linear sweep voltammetry (LSV) curves without *iR* compensation of all electrocatalysts as well as the commercial NF and RuO₂ in N₂-saturated 1.0 M KOH electrolyte with a scan rate of 5.0 mV s⁻¹. It can be seen from Fig. 3a that the NF itself exhibits poor OER activity with an onset potential of 1.56 V (vs.

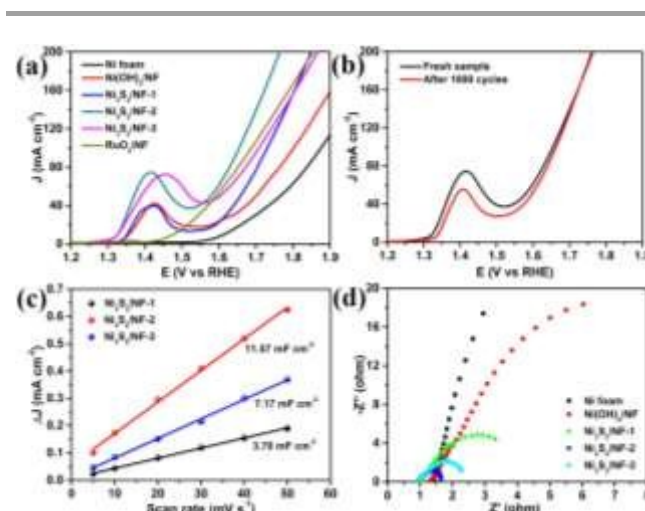


Fig. 3 (a) LSV curves of NF, Ni(OH)₂/NF, Ni₃S₂/NF-1, Ni₃S₂/NF-2, Ni₃S₂/NF-3 and commercial RuO₂ catalysts with a scan rate of 5 mV s⁻¹. (b) OER durability test for the Ni₃S₂/NF-2 electrocatalyst in 1.0 M KOH. (c) Current density as a function of the scan rate for the Ni₃S₂/NF-1, Ni₃S₂/NF-2 and Ni₃S₂/NF-3 catalysts. (d) EIS spectra of NF, Ni(OH)₂/NF, Ni₃S₂/NF-1, Ni₃S₂/NF-2 and Ni₃S₂/NF-3 catalysts.

RHE) and an overpotential of 645 mV in a current density of 100 mA cm⁻², while the commercial RuO₂ shows higher OER activity with an onset potential of 1.41 V (vs. RHE) and an overpotential of 456 mV in a current density of 100 mA cm⁻². Comparatively, obvious oxidation peaks in the potential range of 1.39~1.45 V (vs. RHE) can be first observed for the Ni(OH)₂/NF, Ni₃S₂/NF-1, Ni₃S₂/NF-2 and Ni₃S₂/NF-3 catalysts, which are mainly attributed to the electrochemical oxidation of Ni²⁺ to Ni³⁺.^{39,41,42} Subsequently happened OER processes show that the onset potentials are 1.55, 1.54, 1.52 and 1.55 V (vs. RHE) for the Ni(OH)₂/NF, Ni₃S₂/NF-1, Ni₃S₂/NF-2 and Ni₃S₂/NF-3 respectively, indicating that the Ni₃S₂/NF-2 possesses higher OER activity compared to the Ni(OH)₂/NF, Ni₃S₂/NF-1 and Ni₃S₂/NF-3 catalysts. Moreover, the Ni₃S₂/NF-2 can deliver a high current density of 100 mA cm⁻² at lower overpotential of 425 mV compared to other Ni(OH)₂/NF, Ni₃S₂/NF-1, Ni₃S₂/NF-3, commercial NF and RuO₂ catalysts, further confirming its superior OER performance. Furthermore, Table S1 (ESI[†]) displays a more detailed comparison on OER performance of Ni₃S₂/NF-2 and other reported transition metal based electrocatalysts.^{40-42,44-49} The ultrathin nanosheet array structure of the Ni₃S₂/NF-2 may contribute highly exposed catalytic active sites and superior conductivity for high OER performance. Fig. 3b shows the cycling stability measurement of Ni₃S₂/NF-2. The LSV curve without *iR* compensation after 1000 CV cycles with a potential scan range from 1.2 V~1.4 V vs. RHE only indicates a slight decrease in low current density range (e.g., the OER activity decay in 100 mA cm⁻² is only ~2.8%), while there is no obvious change of the OER activity in high current density range, suggesting its high applicable stability. In this work, the electrochemically active surface area (ECSA) of as-fabricated Ni₃S₂/NF-1, Ni₃S₂/NF-2 and Ni₃S₂/NF-3 catalysts is also evaluated by their electrochemical double-layer capacitance (*C*_{dl}) in a non-Faradaic current region from 0.975 to 1.075 V vs. RHE to get insight into their OER activity.¹⁷ As shown in Fig. S7 (ESI[†]), the Ni₃S₂/NF-2 displays higher current density in comparison with

Ni₃S₂/NF-1 and Ni₃S₂/NF-3 at the same scan rate, implying its larger *C*_{dl} value. As a result, the obtained *C*_{dl} value of the Ni₃S₂/NF-2 is ~11.5 mF cm⁻² (Fig. 3c), significantly higher than that of the Ni₃S₂/NF-1 and Ni₃S₂/NF-3 (3.7 and 7.2 mF cm⁻² respectively, Fig. 3c). The higher ECSA of Ni₃S₂/NF-2 implies its larger functional surface area, thus resulting in its superior OER activity.⁴⁰ Fig. 3d shows the electrochemical impedance spectroscopy (EIS) analysis of as-fabricated Ni(OH)₂/NF, Ni₃S₂/NF-1, Ni₃S₂/NF-2 and Ni₃S₂/NF-3 catalysts as well as the commercial NF. As shown, the Ni₃S₂/NF-2 exhibits the smallest semicircle radius among all investigated electrodes, indicating its smallest charge transfer impedance and superior electrocatalytic activity, consistent with other characterization results.

The superior OER activity of the Ni₃S₂/NF-2 can be ascribed to its ultrathin nanosheet array structure with highly exposed catalytic active sites and good charge transfer capability. Such structure feature of the Ni₃S₂/NF-2 may also favour electrocatalytic oxidation of organics. Therefore, hydrazine was selected as a substance for evaluating the electrocatalytic oxidation activity of the as-fabricated electrocatalysts. Fig. 4a shows the electrocatalytic hydrazine oxidation reaction (HzOR) activity of bare NF, Ni(OH)₂/NF, Ni₃S₂/NF-1, Ni₃S₂/NF-2 and Ni₃S₂/NF-3 in 1.0 M KOH with 0.2 M hydrazine. The LSV curves without *iR* compensation of all investigated electrocatalysts indicate that the onset potentials are 0.78, 0.40, 0.23, 0.10 and 0.17 V (vs. RHE) for the NF, Ni(OH)₂/NF, Ni₃S₂/NF-1, Ni₃S₂/NF-2 and Ni₃S₂/NF-3, respectively. Obviously, the Ni₃S₂/NF catalysts all exhibit higher HzOR activity compared to the bare NF and Ni(OH)₂/NF, possibly owing to a synergistic effect of their composition and unique structure. Furthermore, the Ni₃S₂/NF-2 exhibits the best HzOR activity among all catalysts. More importantly, the introduction of hydrazine in 1.0 M KOH solution results in dramatically decreased oxidation half-reaction potential for all investigated catalysts compared to their corresponding OER process (Fig. 3a), suggesting their more favourable HzOR. In detail,

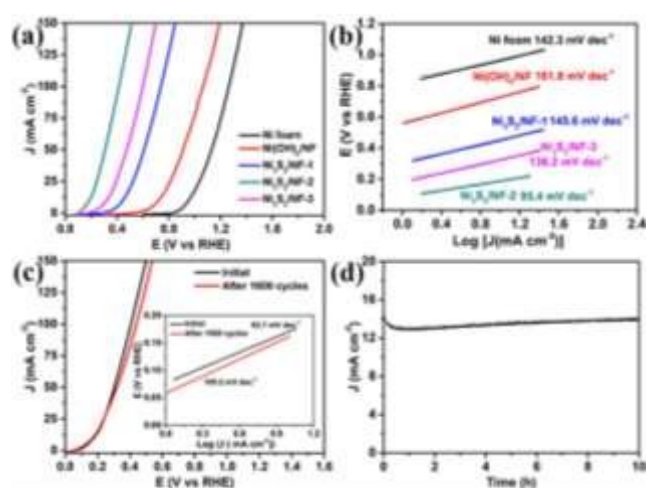


Fig. 4 (a) LSV curves without *iR* drop compensation of NF, Ni(OH)₂/NF, Ni₃S₂/NF-1, Ni₃S₂/NF-2 and Ni₃S₂/NF-3 with 0.2 M hydrazine in 1.0 M KOH. (b) Corresponding Tafel plots. (c) and (d) HzOR stability and durability tests of the Ni₃S₂/NF-2 electrocatalyst in 1.0 M KOH with 0.2 M hydrazine.

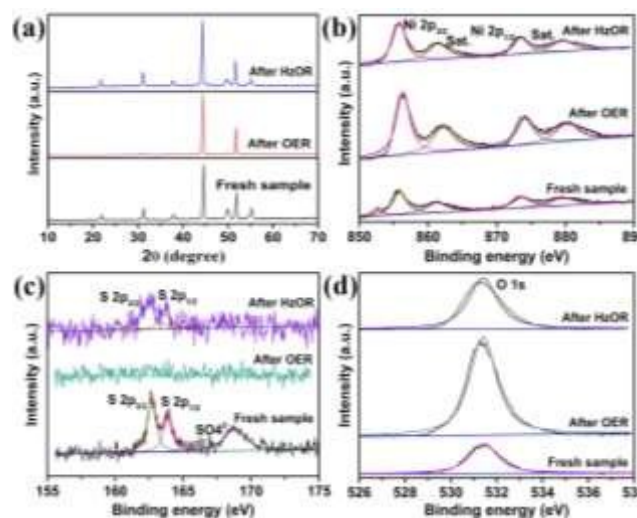


Fig. 5 (a) XRD patterns, (b) XPS Ni 2p, (c) XPS S 2p and (d) XPS O 1s spectrum of Ni₃S₂/NF-2 before (fresh sample) and after long-term HzOR and OER processes.

the potential in a current density of 100 mA cm^{-2} decreases respectively 617, 740, 995, 1240 and 1113 mV for the the NF, $\text{Ni(OH)}_2/\text{NF}$, $\text{Ni}_3\text{S}_2/\text{NF-1}$, $\text{Ni}_3\text{S}_2/\text{NF-2}$ and $\text{Ni}_3\text{S}_2/\text{NF-3}$ in the existence of 0.2 M hydrazine compared to the electrocatalytic water oxidation (OER), further confirming the superior HzOR activity of all electrocatalysts. Moreover, the best HzOR activity can be obtained for the $\text{Ni}_3\text{S}_2/\text{NF-2}$ due to its unique structure. Fig. 4b exhibits the corresponding Tafel slopes of bare NF, $\text{Ni(OH)}_2/\text{NF}$, $\text{Ni}_3\text{S}_2/\text{NF-1}$, $\text{Ni}_3\text{S}_2/\text{NF-2}$ and $\text{Ni}_3\text{S}_2/\text{NF-3}$ catalysts with the values of 142.3, 161.8, 145.6, 95.4 and 136.2 mV dec^{-1} , respectively, suggesting the excellent reaction kinetics of $\text{Ni}_3\text{S}_2/\text{NF-2}$ for HzOR. The stability test of $\text{Ni}_3\text{S}_2/\text{NF-2}$ in 1.0 M KOH with 0.2 M hydrazine demonstrates that the LSV curve of $\text{Ni}_3\text{S}_2/\text{NF-2}$ after 1000 CV cycles at a potential scan range from 0.1 V~0.3 V vs. RHE with a scan rate of 20 mV s^{-1} displays a slight change in current density and corresponding Tafel plots compared to the initial ones, suggesting its good applicable stability (Fig. 4c). Fig. 4d shows the dependence of the current density on the time, indicating that the current density can essentially remain at $\sim 13 \text{ mA cm}^{-2}$ over 10 h at a constant potential of 0.2 V (vs. RHE), further illustrating its good durability. This significantly decreased potential of the oxidation half-reaction owing to the superior HzOR activity may mean that the $\text{Ni}_3\text{S}_2/\text{NF-2}$ can be utilized as an HzOR anode to facilitate the H_2 generation efficiency of the cathode through water splitting. Additionally, the atomic structure and composition of the $\text{Ni}_3\text{S}_2/\text{NF-2}$ can be maintained well at very low HzOR potential, thus capable of establishing the meaningful atomic model for further theoretical study on the catalytic active mechanism.

Many reported works have demonstrated that transitional metal based materials are electrocatalytically active for the OER in alkaline media.^{2-4,21,38} However, their catalytic active mechanisms

are not still very clear owing to the dynamic changes of the catalysts atomic structures and compositions in alkaline media under the operando conditions. The theoretical prediction of the OER active mechanism also experiences a great difficulty because a meaningful atomic structure model of the catalytic active sites cannot be constructed. In this work, we also investigated the change of the crystalline phase and composition of the $\text{Ni}_3\text{S}_2/\text{NF-2}$ before and after the long-term OER and HzOR measurements. Interestingly, it can be found that the Ni_3S_2 phase is still dominant in $\text{Ni}_3\text{S}_2/\text{NF-2}$ after the long-term HzOR measurement, as shown in Fig. 5a. However, the XRD diffraction peaks of the $\text{Ni}_3\text{S}_2/\text{NF-2}$ after the OER are obviously decreased, and some even disappeared compared to the pristine $\text{Ni}_3\text{S}_2/\text{NF-2}$ in alkaline media, implying the surface of Ni_3S_2 possibly transforming into other components. This is consistent with the reported results.^{7,8} Simultaneously, the SEM and TEM images (Fig. S8, ESI[†]) of the $\text{Ni}_3\text{S}_2/\text{NF-2}$ after long-term OER process are also supplied, still exhibiting nanosheet structures with relatively coarse surface compared to the pristine sample, possibly implying the formation of nickel oxides/hydroxides on the surface of the $\text{Ni}_3\text{S}_2/\text{NF-2}$ nanosheets.⁸ Fig. S9 (ESI[†]) shows the surface survey XPS spectra of $\text{Ni}_3\text{S}_2/\text{NF-2}$ before and after the OER and HzOR. It can be seen that C, O, S and Ni elements can be detectable for the $\text{Ni}_3\text{S}_2/\text{NF-2}$ before and after the HzOR, while only C, O and Ni without S can be observed for the $\text{Ni}_3\text{S}_2/\text{NF-2}$ after the OER, further indicating a possible change of the composition and structure of the $\text{Ni}_3\text{S}_2/\text{NF-2}$ during the OER in alkaline media. Fig. 5b shows the high-resolution Ni 2p XPS spectra of $\text{Ni}_3\text{S}_2/\text{NF-2}$ before and after the OER and HzOR. As shown, the two strong peaks at the binding energies of 855.7 and 873.4 eV can be observed for the $\text{Ni}_3\text{S}_2/\text{NF-2}$ before and after the HzOR, attributing to the $\text{Ni } 2p_{3/2}$ and $\text{Ni } 2p_{1/2}$, respectively.^{38,50} Comparatively, these two peaks with obviously enhanced intensity of the $\text{Ni}_3\text{S}_2/\text{NF-2}$ after the OER happen to a slight shift ($\sim 0.4 \text{ eV}$) toward high binding energy, suggesting the formation of high valence-state nickel species, such as oxides, hydroxides and oxyhydroxides during the OER in alkaline media.^{38,50,51} Additionally, the high-resolution S 2p XPS spectra (Fig. 5c) of the $\text{Ni}_3\text{S}_2/\text{NF-2}$ before and after the OER and HzOR exhibit that the peaks of S $2p_{3/2}$ and S $2p_{1/2}$ at the binding energies of 162.5 and 163.7 eV can be detected for the $\text{Ni}_3\text{S}_2/\text{NF-2}$ before and after the HzOR, while the corresponding peaks are almost completely disappeared for the $\text{Ni}_3\text{S}_2/\text{NF-2}$ after the OER with an obviously enhanced O 1s peak intensity (Fig. 5d). The above results

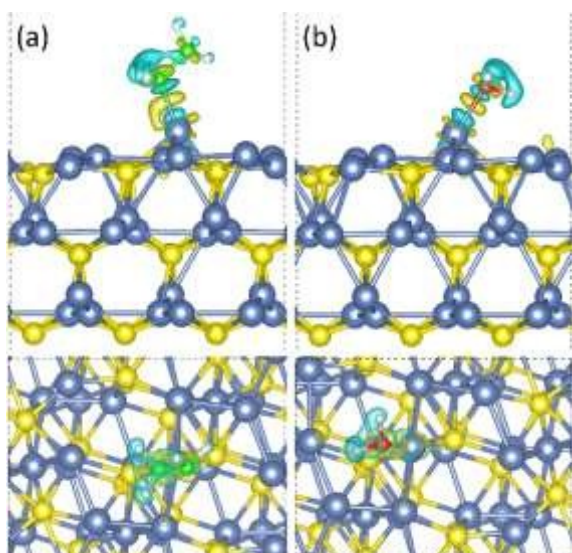


Fig. 6 The differential charge density graph of stable adsorption configurations of N_2H_4 and H_2O molecule with the side (up) and top (down) view, respectively. Ni, S, O, N, and H in light blue, yellow, red, green and white, respectively. Where the yellow and cyan contours indicate the charge accumulations and reductions with the iso-surface value of 0.003 e/bohr^3 , respectively.

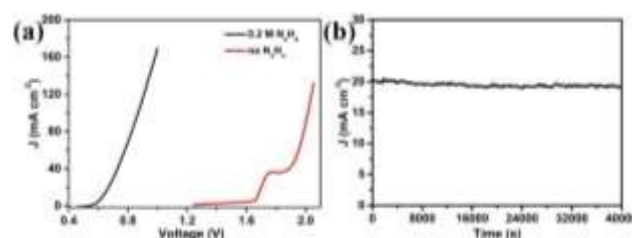


Fig. 7 (a) LSV curves for the $\text{Ni}_3\text{S}_2/\text{NF-2}$ with the presence and absence of 0.2 M hydrazine in 1.0 M KOH using a two-electrode system. (b) Stability test for the $\text{Ni}_3\text{S}_2/\text{NF-2}$ with the presence of 0.2 M hydrazine in 1.0 M KOH with current density of 20 mA cm^{-2} .

demonstrate that the surface structure and composition of the $\text{Ni}_3\text{S}_2/\text{NF}-2$ after the OER may happen to a change owing to higher OER potential, while the $\text{Ni}_3\text{S}_2/\text{NF}-2$ after the HzOR process maintains good surface structure/composition properties as same as the pristine $\text{Ni}_3\text{S}_2/\text{NF}-2$ ascribed to lower HzOR potential.

Owing to well-maintained surface structure and composition of the $\text{Ni}_3\text{S}_2/\text{NF}-2$ after the HzOR obtained at lower oxidation potential, we can therefore construct a meaningful atomic structure model to understand theoretically its superior HzOR activity. The detailed theoretical calculations information is supplied in the experiment section. As we know, the adsorption of reactants on the catalyst surface is a key step for their following electrocatalytic reaction.^{53,27} The corresponding $\text{Ni}_3\text{S}_2(110)$ surface, H_2O and N_2H_4 molecule models are shown in Fig. S2 and Fig. S10 (ESI⁺), respectively. The stable adsorbate configurations of H_2O and N_2H_4 molecules are displayed in Fig. 6 and Fig. S3 (ESI⁺), which bound with a low coordinate Ni atom (Ni-1) through N (O) atom with single-dendate configuration on $\text{Ni}_3\text{S}_2(110)$ surface. The adsorption energy of N_2H_4 on $\text{Ni}_3\text{S}_2(110)$ surface is -1.41 eV, much lower than that (-0.82 eV) of H_2O , as shown in Table S2 (ESI⁺). It means that the interaction between N_2H_4 molecule and $\text{Ni}_3\text{S}_2(110)$ surface is much stronger than H_2O , N_2H_4 will be prior to occupy the surface. Furthermore, Bader charge analysis indicates that N_2H_4 molecule can obtain much more electrons than H_2O molecule by 0.0705 in Table S2 (ESI⁺). After adsorption, the bond length of O-H and bond angle of H-O-H of H_2O are slightly increased from 0.972 Å to 0.985 Å and 104.533° to 105.597°, respectively, in comparison with the free H_2O molecule. For N_2H_4 molecule, the bond length of N-H also increases a little from 1.029 Å to 1.031 Å, but the bond angle of H-N-N and H-N-H increases obviously from 103.871° to 112.625° and 102.403° to 108.814°, respectively. It displays that the $\text{Ni}_3\text{S}_2(110)$ surface can active N_2H_4 molecule enormously than H_2O . More importantly, the bond length of N-N decreased from 1.488 Å to 1.450 Å, approximate to the bond length of N_2 molecule with 1.117 Å, implying that N_2H_4 can be electrocatalytically oxidized to N_2 .⁵³ Last but not least, the desorption of the oxidation products of H_2O and N_2H_4 are also very important. We therefore consider the adsorption of O_2 and N_2 on the $\text{Ni}_3\text{S}_2(110)$ surface, as shown in Fig. S11 (ESI⁺). The DFT calculations results indicate that the adsorption energy of N_2 on the $\text{Ni}_3\text{S}_2(110)$ surface is -0.97 eV, obviously higher than that (-1.41 eV) of N_2H_4 by 0.44 eV while lower than that (-0.82 eV) of H_2O by -0.15 eV. It means that the oxidation product (N_2) of N_2H_4 can easily desorb from the $\text{Ni}_3\text{S}_2(110)$ surface, thus leaving the active sites. Although the adsorption energy of O_2 on the $\text{Ni}_3\text{S}_2(110)$ surface is -1.42 eV, the lowest value among all, H_2O cannot be captured by the surface in the presence of hydrazine.

To announce the bond mechanism of H_2O and N_2H_4 molecules with $\text{Ni}_3\text{S}_2(110)$ surface, their band decomposed charge densities around the Fermi level were calculated, as illustrated by Fig. S12 (ESI⁺). For the $\text{Ni}_3\text{S}_2(110)$ surface, the Ni exposed surface exhibits much more charge distribution than S exposed layer surface, and Ni-1 atoms have much more charge distribution than high coordinate Ni atoms (Ni-2). The highest occupied molecule orbital (HOMO) and lowest unoccupied molecule orbital (LUMO) of H_2O

and N_2H_4 molecules were mainly contributed by O and N atoms in Fig. S12 (ESI⁺), respectively. They could also explain the adsorption configurations of H_2O and N_2H_4 molecules, namely, the N (O) atom of N_2H_4 (H_2O) bound with Ni-1 atom. The differential charge density analysis shows that N_2H_4 adsorption exists much more orbital overlap than H_2O adsorption in the Fig. 6. It demonstrates that the N_2H_4 molecules are readily adsorbed and activated on the $\text{Ni}_3\text{S}_2(110)$ surface, thus contributing high HzOR activity at lower oxidation potential.

Additionally, we also find that the as-fabricated $\text{Ni}_3\text{S}_2/\text{NF}-2$ possesses high electrocatalytic activity toward the hydrogen evolution reaction (HER) in 1.0 M KOH electrolyte. Fig. S13a (ESI⁺) shows the LSV curves for HER of bare NF, $\text{Ni}(\text{OH})_2/\text{NF}$, $\text{Ni}_3\text{S}_2/\text{NF}-1$, $\text{Ni}_3\text{S}_2/\text{NF}-2$, $\text{Ni}_3\text{S}_2/\text{NF}-3$ and commercial Pt/C coated on NF electrode in 1.0 M KOH. Apparently, the $\text{Ni}_3\text{S}_2/\text{NF}-2$ exhibits the best HER activity with an onset potential of -0.05 V (vs. RHE) and an overpotential of 225 mV in 100 mA cm⁻², among all investigated catalysts except for the commercial Pt/C. The HER property of $\text{Ni}_3\text{S}_2/\text{NF}-2$ is comparable to the recently reported Ni-based catalysts, such as NiCo_2S_4 NW/NF (210 mV @ 10 mA cm⁻²),⁵⁴ NiCo alloy (193 mV @ 10 mA cm⁻²),⁹ Ni_3S_2 (170 mV @ 10 mA cm⁻²),⁵⁵ NiCo_2O_4 alloy (245 mV @ 100 mA cm⁻²),⁵⁶ Ni_3S_2 -based (224 mV @ 100 mA cm⁻²),⁵⁷ $\text{Ni}_{0.7}\text{Fe}_{0.3}\text{S}_2$ (305 mV @ 100 mA cm⁻²)⁵⁸ and other literatures.^{59,60} Also, the $\text{Ni}_3\text{S}_2/\text{NF}-2$ displays superior kinetic reaction for the HER (Fig. S13b, ESI⁺) and high applicable stability and durability (Fig. S13c, d, ESI⁺). The high HER activity combined with its superior HzOR activity makes the $\text{Ni}_3\text{S}_2/\text{NF}-2$ promising as anode and cathode catalyst for the water splitting to facilitate H_2 generation. Simultaneously, the absence of hydrazine shows ignorable affect HER property of $\text{Ni}_3\text{S}_2/\text{NF}-2$ sample (Fig. S14, ESI⁺). For this, we constructed a two-electrode system assembled with the $\text{Ni}_3\text{S}_2/\text{NF}-2$ as both anode and cathode for water splitting to generate H_2 in 1.0 M KOH containing 0.2 M hydrazine. Fig. 7a shows the LSV curves without *iR* compensation of $\text{Ni}_3\text{S}_2/\text{NF}-2$ in 1.0 M KOH containing 0.2 M hydrazine. This two-electrode system also shows superior HzOR performance, capable of delivering a current density of 100 mA cm⁻² at an applied voltage of 0.867 V, while the applied voltage is 2.01 V to achieve the same current density without the presence of hydrazine in 1.0 M KOH. Obviously, the introduction of hydrazine in 1.0 M KOH electrolyte can effectively decrease the potential of oxidation half-reaction in a two-electrode system, meaning significantly enhanced H_2 generation through water splitting on the $\text{Ni}_3\text{S}_2/\text{NF}-2$ cathode. Moreover, as shown in Fig. 7b, the stability test indicates that the current density can essentially maintain at around 20 mA cm⁻² after 10 h reaction in such two-electrode system, suggesting its high applicable durability. Moreover, a two-electrode system with an applied potential of 0.75 V is constructed to perform the HzOR (0.2 M) experiment for H_2 generation, exhibiting a current of ~38.5 mA (Fig. S15, ESI⁺). As shown in Fig. S16 (ESI⁺), the H_2 and N_2 evolution rates of this two-electrode system are respectively 11.83 and 5.90 μmol min⁻¹ with a nearly unity Faradaic efficiency (~100%). The above results demonstrate that replacing OER by HzOR using $\text{Ni}_3\text{S}_2/\text{NF}-2$ as the

oxidation half-reaction in a water splitting system should be a very effective strategy to facilitate the H₂ generation.

Conclusions

In summary, three-dimensional nickel foam supported ultrathin Ni₃S₂ nanosheets electrocatalyst with the nanosheet thickness of 9~14 nm is successfully fabricated *via* a VPH approach. The as-prepared Ni₃S₂/NF-2 exhibits multifunctional electrocatalytic activities, promising for energy-saving electrocatalytic H₂ evolution in alkaline media through replacing OER by HzOR. The Ni₃S₂/NF-2 constructs two-electrode system can afford 100 mA cm⁻² at a voltage of 0.867 V with high long-term durability in 1.0 M KOH with 0.2 M hydrazine. The DFT calculations indicate that N₂H₄ molecules are more thermodynamic favourable for occupying the active Ni atom sites of Ni₃S₂ than H₂O. This work demonstrates the feasibility of using transition metal-based electrocatalysts integrating more superior fuel molecules oxidation reaction for energy-saving electrochemical water splitting to generate clean H₂.

Acknowledgements

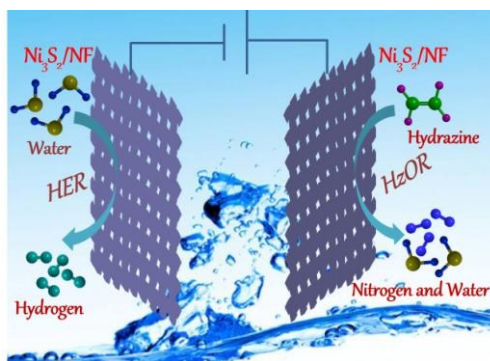
This work was financially supported by the Natural Science Foundation of China (Grant No. 51672277 and 51432009), the CAS/SAFEA International Partnership Program for Creative Research Teams of Chinese Academy of Sciences, China, and the CAS Pioneer Hundred Talents Program.

Notes and references

- Z. F. Huang, J. Wang, Y. C. Peng, C. Y. J, A. Fisher, X. Wang, *Adv. Energy Mater.*, 2017,7,1700544.
- G. Zhang, G. C. Wang, Y. Liu, H. J. Liu, J. H. Qu, J. H. Li, *J. Am. Chem. Soc.*, 2016, 138, 14686–14693.
- D. V. Shinde, L. D. Trizio, Z. Y. Dang, M. Prato, R. Gaspari, L. Manna, *Chem. Mater.*, 2017, 29, 7032-7041.
- X. L. Yang, H. N. Li, A. Y. Lu, S. X. Min, Z. Idriss, M. N. Hedhili, K. W. Huang, H. Idriss, L. J. Li, *Nano Energy*, 2016, 25,42-50.
- S. Y. Tee, K. Y. Win, W. S. Teo, L. D. Koh, S. H. Liu, C. P. Teng, M. Y. Han, *Adv. Sci.*, 2017, 6, 1600337.
- W. J. Zhou, X. J. Wu, X. H. Cao, X. Huang, C. L. Tan, J. Tian, H. Liu, J. Y. Wang, H. Zhang, *Energy Environ. Sci.*, 2013, 6, 2921-2924.
- B. You, X. Liu, N. Jiang, Y. J. Sun, *J. Am. Chem. Soc.*, 2016, 138, 13639-13646.
- B. You, N. Jiang, X. Liu, Y. J. Sun, *Angew. Chem., Int. Ed.*, 2016, 55, 9913-9917.
- G. Q. Liu, X. Zhang, C. J. Zhao, Q. Z. Xiong, W. B. Gong, G. Z. Wang, Y. X. Zhang, H. M. Zhang, H. J. Zhao, *New J. Chem.*, 2018, 42, 6381-6388.
- N. Jiang, B. You, R. Boonstra, I. M. T. Rodriguez, Y. J. Sun, *ACS Energy Lett.*, 2016, 1, 386-390.
- H. G. Cha, K. S. Choi, *Nat. Chem.*, 2015, 7, 328-333.
- X. Zhang, Y. Y. Liu, Q. Z. Xiong, G. Q. Liu, C. J. Zhao, G. Z. Wang, Y. X. Zhang, H. M. Zhang, H. J. Zhao, *Electrochimica Acta*, 2017, 254, 44-49.
- U. Martinez, K. Asazawa, B. Halevi, A. Falase, B. Kiefer, A. Serov, M. Padilla, T. Olson, A. Datye, H. Tanaka, P. Atanassov, *Phys. Chem. Chem. Phys.*, 2012, 14, 5512-5517.
- Z. Y. Lu, M. Sun, T. H. Xu, Y. J. Li, W. W. Xu, Z. Chang, Y. Ding, X. M. Sun, L. Jiang, *Adv. Mater.*, 2015, 27, 2361-2366.
- Y. Wang, B. Kong, D. Y. Zhao, H. T. Wang, *ACS Nano*, 2017, 15, 26-55.
- Y. Yan, B. Y. Xia, B. Zhao, X. Wang, *J. Mater. Chem. A*, 2016, 4, 17587-17603.
- T. X. Wu, X. G. Zhu, G. Z. Wang, Y. X. Zhang, H. M. Zhang, H. J. Zhao, *Nano Res.*, 2018, 11, 1004-1017.
- P. R. Liu, H. M. Zhang, H. W. Liu, Y. Wang, X. D. Yao, G. S. Zhu, S. Q. Zhang, H. J. Zhao, *J. Am. Chem. Soc.*, 2011, 133, 19032-19035.
- P. R. Liu, Y. Wang, H. M. Zhang, T. C. An, H. G. Yang, Z. Y. Tang, W. P. Cai, H. J. Zhao, *Small*, 2012, 8, 3664-3673.
- J. X. Feng, J. Q. Wu, Y. X. Tong, G. R. Li, *J. Am. Chem. Soc.*, 2018, 140, 610-617.
- L. L. Feng, G. T. Yu, Y. Y. Wu, G. D. Li, H. Li, Y. H. Sun, T. Asefa, W. Chen, X. X. Zou, *J. Am. Chem. Soc.*, 2015, 137, 14023-14026.
- B. L. Hua, X. Y. Qin, A. M. Asiri, K. A. Alamry, A. O. Youbi, X. P. Sun, *Electrochimica Acta*, 2013, 107, 339-342.
- G. Kresse, J. Furthmüller, *Comp. Mater. Sci.*, 1996, 6, 15-22.
- G. Kresse, J. Furthmüller, *Phys. Rev. B*, 1996, 54, 11169-11186.
- P. E. Blöchl, *Phys. Rev. B*, 1994, 50, 17953-17960.
- J. P. Perdew, K. Burke, M. Ernzerhof, *Phys. Rev. Lett.*, 1996, 77, 3865-3868.
- H. J. Monkhorst, J. D. Pack, *Phys. Rev. B*, 1976, 13, 5188-5192.
- W. Tang, E. Sanville, G. Henkelman, *J. Phys.: Condens. Mat.*, 2009, 21, 084204-084211.
- W. X. Zhu, X. Y. Yue, W. T. Zhang, S. X. Yu, Y. H. Zhang, J. Wang, J. L. Wang, *Chem. Commun.*, 2016, 52,1486-1489.
- R. R. Salunkhe, J. J. Lin, V. Malgr, S. X. Dou, J. H. Kim, Y. Yamauchi, *Nano Energy*, 2015, 11, 211-218.
- J. S. Chen, C. Guan, Y. Gui, D. J. Blackwood, *ACS Appl. Mater. Interfaces*, 2017, 9, 496-504.
- J. Q. Qi, Y. Chang, Y. W. Sui, Y. Z. He, Q. K. Meng, F. X. Wei, Y. J. Ren, Y. X. Jin, *Adv. Mater. Interfaces*, 2018, 5, 1700985.
- M. C. Bernard, R. Cortes, M. Keddani, H. Takenouti, P. Bernard, S. Senyari, *J. Power Sources*, 1996, 63, 247-254.
- Z. Cheng, H. Abernathy, M. L. Liu, *J. Phys. Chem. C*, 2007, 111, 17997-18000.
- P. Hu, T. S. Wang, J. W. Zhao, C. J. Zhang, J. Ma, H. P. Du, X. G. Wang, G. L. Cui, *ACS Appl. Mater. Interfaces*, 2015, 7, 26396-26399.
- S. Chen, Y. L. Xin, Y. Y. Zhou, Y. R. Ma, H. H. Zhou, L. M. Qi, *Energy Environ. Sci.*, 2014, 7, 1924-1930.
- C. Zhou, Y. F. Zhao, L. Shang, R. Shi, L. Z. Wu, C. H. Tung, T. R. Zhang, *Chem. Commun.*, 2016, 52, 8239-8242.
- W. J. Zhou, X. J. Wu, X. H. Cao, X. Huang, C. L. Tan, J. Tian, H. Liu, J. Y. Wang, H. Zhang, *Energy Environ. Sci.*, 2013, 6, 2921-2924.
- W. D. He, C. G. Wang, H. Q. Li, X. L. Deng, X. J. Xu, T. Y. Zhai, *Adv. Energy Mater.*, 2017, 7, 1700983.
- X. Q. Du, H. L. Pan, Z. Yang, *New J. Chem.*, 2018, 42, 4215-4222.
- X. Q. Du, Z. Yang, Y. Li, Y. Q. Gong, M. Zhao, *J. Mater. Chem. A*, 2018, 6, 6938-6946.
- X. Q. Du, Q. B. Wang, Y. Li, X. S. Zhang, *Dalton T.*, 2018, 47, 10273-10280.
- X. Q. Du, J. W. Huang, Y. Ding, *Dalton T.*, 2017, 46, 7327-7331.
- X. X. Guo, S. Y. Zhu, R. M. Kong, X. P. Zhang, F. L. Qu, *ACS Sustain. Chem. Eng.*, 2018, 6, 1545-1549.
- X. P. Zhang, C. D. Si, X. X. Guo, R. M. Kong, F. L. Qu, *J. Mater. Chem. A*, 2017, 5, 17211-17215.
- X. X. Guo, R. M. Kong, X. P. Zhang, H. T. Du, F. L. Qu, *ACS Catal.*, 2017, 8, 651-655.
- W. Z. Fang, D. N. Liu, Q. Lu, X. P. Sun, A. M. Asiri, *Electrochem. Commun.*, 2016, 63, 60-64.

- 48 N. Jiang, B. You, M. L. Sheng, Y. J. Sun, *Angew. Chem., Int. Ed.*, 2015, 127, 6349-6352.
- 49 T. T. Liu, Y. H. Liang, Q. Liu, X. P. Sun, Y. Q. He, A. M. Asiri, *Electrochem. Commun.*, 2015, 60, 92-96.
- 50 B. You, Y. J. Sun, *Adv. Energy Mater.*, 2016, 6, 1502333.
- 51 N. Jiang, X. Liu, J. M. Dong, B. You, X. Liu, Y. J. Sun, *ChemNanoMat*, 2017, 3, 491-495.
- 52 X. Zhang, Y. F. Zhao, X. D. Jia, Y. X. Zhao, L. Shang, Q. Wang, G. I. N. Waterhouse, L. Z. Wu, C. H. Tung, T. R. Zhang, *Adv. Energy Mater.*, 2018, 8, 1702780.
- 53 L. Zhou, M. F. Shao, C. Zhang, J. W. Zhao, S. He, D. M. Rao, M. Wei, D.G. Evans, X. Duan, *Adv. Mater.*, 2017, 29, 1604080.
- 54 A. Sivanantham, P. Ganesan, S. Shanmugam, *Adv. Funct. Mater.*, 2016, 26, 4661-4672.
- 55 L. L. Feng, G. T. Yu, Y. Y. Wu, G. D. Li, H. Li, Y. H. Sun, T. Asefa, W. Chen, X. X. Zou, *J. Am. Chem. Soc.*, 2015, 137, 14023-14026.
- 56 X. H. Gao, H. X. Zhang, Q. G. Li, X. G. Yu, Z. L. Hong, X. W. Zhang, C. D. Liang, Z. Lin, *Angew. Chem. Int. Edit.*, 2016, 128, 6398-6402.
- 57 Y. Y. Wu, G. D. Li, Y. P. Liu, L. Yang, X. R. Lian, T. Asefa, X. X. Zou, *Adv. Funct. Mater.*, 2016, 26, 4839-4847.
- 58 J. H. Yu, G. Z. Cheng, W. Luo, *J. Mater. Chem. A*, 2017, 5, 15838-15844.
- 59 X. P. Zhang, S. Y. Zhu, L. Xia, C. D. Si, F. Qu, F. L. Qu, *Chem. Commun.*, 2018, 54, 1201-1204.
- 60 H. T. Du, L. Xia, S. Y. Zhu, F. Qu, F. L. Qu, *Chem. Commun.*, 2018, 54, 2894-2897.

View Article Online
DOI: 10.1039/C8TA07162D



View Article Online
DOI: 10.1039/C8TA07162D

Ultrathin Ni_3S_2 nanosheets grown on nickel foam ($\text{Ni}_3\text{S}_2/\text{NF}$) is thermodynamically favourable for the hydrazine adsorption, exhibiting superior hydrazine oxidation activity and high-efficiency H_2 generation in $\text{Ni}_3\text{S}_2/\text{NF}$ assembled two-electrode system.